COMMUNICATION

The glass transition in the high-density amorphous Zn/Co-ZIF-4

Zijuan Du,[acd] Ang Qiao,[a] Hemin Zhou,[a] Zhencai Li,[b] Wessel M. W. Winters,[b] Jiexin Zhu,[d] Guanjie He,[d] Ivan P. Parkin,[c] Haizheng Tao*[a] and Yuanzheng Yue*[b]

Received 00th January 20xx,
Accepted 00th January 20xx

DOI: 10.1039/x0xx00000x

The high-density amorphous phases (HDAs) of bimetallic zeolitic imidazolate frameworks (Zn/Co-ZIF-4) were prepared. The temperature dependence of the isobaric heat capacity (C_p) of ZIF-4 HDAs was measured to determine the glass transition temperature (T_g) of HDAs. The T_g non-linearly decreases with the molar ratio *R*, where *R* is Co/(Co+Zn), indicating the presence of a mixed-metal node effect. This effect arises from the non-linear increase of the degree of configurational freedom in the HDA as *R* increases. The degree of configurational freedom is inversely correlated with the network connectivity, which is, in turn, affected by variations in the MN_4 (M: Zn or Co; N: nitrogen) tetrahedral symmetry in the ZIF-4 HDA. Overall, this work offers valuable insights into the glass transition of metal-organic frameworks.

Metal-organic frameworks (MOFs) with structural designability and compositional diversity, emerging as new glass formers, have great potential in various applications.[1-3] As a subset of MOFs, zeolitic imidazolate frameworks (ZIFs) have captured considerable interest owing to their high thermal and chemical stabilities.[4-7] Some of the ZIFs, such as ZIF-4 [$M(Im)_2$, M = transition metal node, Im (imidazolate) linker= $C_3H_3N_2^-$], can be transformed into network glasses via melt-quenching.[7-11] Specifically, upon heating, ZIF-4 experiences a polyamorphic transition, i.e., a transformation of a "super-strong (in fragility)" low-density liquid into a relatively "fragile" high-density liquid.[12] By cooling, the latter is transformed into a glass state, i.e., high-density amorphous phase (HDA). By reheating the quenched HDA, the glass-to-liquid transition occurs. The pair distribution functions confirmed that the organic ligand and zinc tetrahedral coordination environments of ZIF-4 were retained in the HDA.[12] Recently, it was reported that the cyano(CN)-functionalized ZIF-4 underwent a polyamorphic transition.[13] Additionally, the electron-withdrawing CN groups weaken the Zn-N bonds, leading to a lower glass transition temperature (T_g) of the CN-functionalized HDA compared to the prototypical ZIF-4 HDA.

Understanding the connection between the glass transition and structural factors is crucial for the successful liquid-phase processing of ZIFs to achieve desired properties in ZIF glasses.[6,13] Besides the linker exchange strategy, the substitution of metal nodes in ZIFs can also affect the formation and structural properties of these ZIF glasses.[14,15] For instance, the substitution of Co for Zn in ZIF-62 caused a mixed-metal node effect, i.e., a negative deviation from the linearity of the T_g versus the molar ratio *R* (Co/(Co+Zn)).[14] This deviation was attributed to a structural mismatch and electronic configurational difference between Co^{2+} and Zn^{2+}. The mixed-metal node effect is important for creating functionalities in ZIF glasses, e.g., electrochemical functions,[16,17] luminescence,[18] and gas separation[19]. The exploration of new ZIF glasses offers opportunities to expand their applications. All these aspects motivate us to investigate the mixed-metal node effect in the HDAs of ZIF-4, which, to the best of our knowledge, has not been reported thus far. In this work, we prepared bimetallic Zn/Co-ZIF-4 crystals and then investigated the mixed-metal node effect in their HDAs with respect to the T_g values.

A solvothermal method (see ESI† for details) was used to synthesize a series of ZIFs with various Co/(Co+Zn) molar ratios. The chemical composition of bimetallic ZIFs samples was determined by inductively coupled plasma optical emission spectrometry (ICP-OES). Elemental analysis in Table S1 (ESI†) indicates the simultaneous incorporation of zinc and cobalt ions in the ZIFs structure. The percentage of Co incorporated in the ZIFs structure indeed increases with cobalt concentration during the synthesis process. Remarkably, the measured molar ratios (*R*) of Co/(Co+Zn) are all lower than the nominal ones. For instance, for a nominal molar ratio x of Co/(Co+Zn) to be 0.8, the *R* in the as-prepared product is only 0.59. From the ICP-OES experimental data, we infer that the incorporation of Zn is thermodynamically more favoured than that of Co in the ZIFs framework.[20] Moreover, as shown in Fig. S1, the powder X-ray

[a] State Key Laboratory of Silicate Materials for Architectures (Wuhan University of Technology), Wuhan 430070, China.
[b] Department of Chemistry and Bioscience, Aalborg University, DK-9220 Aalborg, Denmark.
[c] Christopher Ingold Laboratory, Department of Chemistry, University College London, London WC1H 0AJ, UK.
[d] Electrochemical Innovation Lab (EIL), Department of Chemical Engineering, University College London, London WC1E 7JE, UK.

† Footnotes relating to the title and/or authors should appear here.
Electronic Supplementary Information (ESI) available: [details of any supplementary information available should be included here]. See DOI: 10.1039/x0xx00000x

diffraction (PXRD) patterns of the as-synthesized ZIFs are consistent with the simulated ones of the ZIF-4(Zn/Co). This indicates that the samples are highly crystalline and that the synthesized bimetallic $Zn_{1-R}Co_R$-ZIF-4 crystals possess the cag topology structure[5] for the parent ZIF-4 framework. Additionally, the intensity of the X-ray diffraction peaks for the bimetallic Zn,Co-ZIF-4 and pure Co_1-ZIF-4 is lower than that of the pure Zn_1-ZIF-4 peak. This is because the fluorescence induced during measurements is stronger for the Co-containing ZIF samples than for the Zn-ZIF-4 sample.[21] According to the Hume-Rothery rule, a solid solution can form via the substitution of Co for Zn in the Zn-ZIF-4 framework.[22] Specifically, Zn and Co elements have a relative difference in atomic sizes of less than 15% (Shannon radii: 0.60 Å for Zn^{2+} and 0.58 Å for Co^{2+})[23] and similar electronegativities (1.65 Å for Zn and 1.88 Å for Co)[24]. In Fig. 1, the four XRD peaks A, B, C, and D in the range of 7-15° of each bimetallic $Zn_{1-R}Co_R$-ZIF-4 crystal exhibit a slight shift compared to the Zn_1/Co_1-ZIF-4, indicating that four bimetallic ZIF-4 crystals possess unique cell parameters due to the solid solution formation.[25]

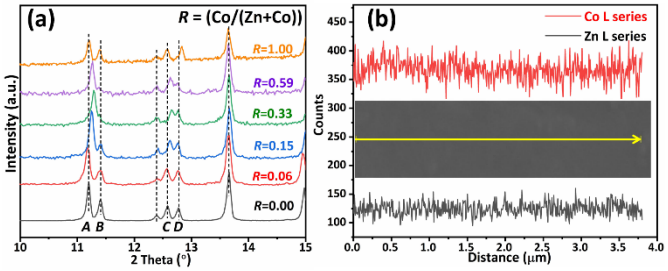

Fig. 1. (a) PXRD patterns of the as-synthesized ZIFs with *R* (=Co/(Co+Zn)). The patterns have been normalized and offset vertically for clarity. (b) EDS line scan profiles of the bimetallic $Zn_{1-R}Co_R$-ZIF-4 crystal with *R*=0.59 along the yellow line shown in the field emission scanning electron microscopy (FESEM) image (inset).

For the surface composition analysis, energy dispersive spectroscopy (EDS) line and mapping scan analyses were conducted on the bimetallic ZIF-4 crystals. Fig. 1b shows the elemental concentration profiles along the arrowed line of the bimetallic ZIF-4 crystal with *R* = 0.59, i.e., $Zn_{0.41}Co_{0.59}(C_3H_3N_2)_2$, where the counts for Zn and Co elements have similar intensity in the tested ZIF-4 domain. This confirms that the Zn and Co elements are homogeneously distributed at the micron scale in the ZIF-4 without noticeable aggregation. The elemental mapping images and EDS spectra of the bimetallic ZIF-4 crystals, shown in Figs. S2-S9 (ESI†), further prove that the synthesized bimetallic ZIF-4 crystals are all composed of Zn, Co, C and N elements. All these results indicate the coexistence of Zn and Co in the bimetallic crystals, confirming the formation of a solid solution of ZIF-4(Zn) framework and ZIF-4(Co) framework and not a physical mixture of both.[20,21] The thermal behaviour of the ZIF-4 powder is examined via thermogravimetry (TG) and differential scanning calorimetry (DSC). The solid curves in the region of 100-380 °C in Fig. S10 (ESI†) show desolvation, polyamorphization, recrystallization (towards the dense ZIF-zni phase), and subsequent melting and decomposition events, similar to the previously reported results.[7,26] For ZIF-4 crystals, the TG curves (Fig. S10, ESI†) show the loss of the DMF solvent molecules trapped within the porous cavities of the ZIF-4 upon heating to 270 °C. This resulted in the formation of solvent-free ZIF-4 crystals, with no indications of structural collapse. On raising the temperature, the signatures of the amorphization become visible and the process starts with a specific Zn-N bond reconstruction.[12] Subsequently, quenching from 380 °C without isothermal treatment leads to the formation of the HDAs with the same thermal history, i.e., a cooling rate of 10 °C min^{-1}. PXRD confirms the amorphous nature of HDAs (Fig. S11, ESI†). Elemental compositions and distribution of the HDAs were identified by EDS mapping. Uniform distribution of the metal element (Zn or Co), C and N for Zn_1-HDA (*R* = 0.00) and Co_1-HDA (*R* = 1.00) is observed in Figs. S12-S13 (ESI†). In addition, Figs. S14-S17 (ESI†) demonstrate the co-existence of Zn, Co, C, and N elements in all the bimetallic HDAs, confirming the homogeneous distribution of Zn and Co throughout the bimetallic HDAs.

Fourier transform infrared (FTIR) absorption spectra of the HDAs were collected to identify the functional groups in the structure (Fig. S18, ESI†). The peaks at 669 cm^{-1} relating to the ring deformations of the Im organic linkers in the HDAs are all present.[27] Moreover, the stretching vibrations of C-H (~3128 cm^{-1}), C=C (~1670 cm^{-1}), C=N (~1597 cm^{-1}), and C-N (~1315 cm^{-1}) bands in imidazole remain in the HDAs.[28] This implies that the imidazole linkers remain unchanged during amorphization. The element chemical states of the HDAs were investigated by X-ray photoelectron spectroscopy (XPS). The survey spectra in Fig. S19a (ESI†) show the peaks belonging to Zn, Co, C and N elements, confirming their co-existence. The peaks near 1021.7 and 1044.8 eV (Fig. S19b, ESI†) correspond to the binding energies of Zn^{2+} $2p_{3/2}$ and Zn^{2+} $2p_{1/2}$.[29] In Fig. S19c (ESI†), the peaks at 781.5 and 796.9 eV can be assigned to Co $2p_{3/2}$ and Co $2p_{1/2}$, matching with the spin-orbit characteristic of Co^{2+}.[30] Two shakeup satellites (identified as "Sat.") are located at 802.7 and 786.7 eV.[30] The above results indicate that Co^{2+} and Zn^{2+} coexist in the bimetallic HDAs.

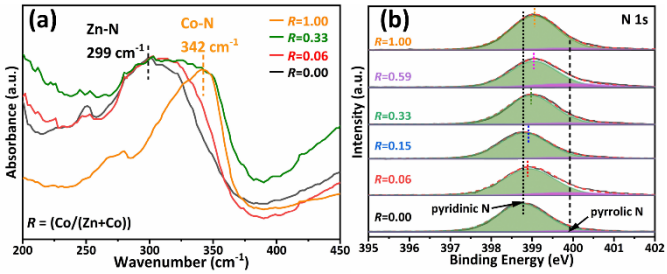

Fig. 2. (a) Far-FTIR spectra and (b) N 1s high-resolution XPS spectra of the bimetallic $Zn_{1-R}Co_R$-HDAs with different *R*. In (b), the experimental and total fits are shown as black solid and red dashed lines, respectively; the peak areas filled with green and purple colors denote pyridinic N and pyrrolic N species, respectively. The spectra have been offset vertically for clarity.

To probe the bonding environments of the HDAs, the far-FTIR spectroscopy measurement was carried out. The FTIR spectra in the region 200-450 cm^{-1} of HDAs are shown in Fig. 2a. The peak, which is associated with the shared Zn-N bond stretching motion originating from the compliance of $Zn(Im)_4$ tetrahedra, is positioned at 265-325 cm^{-1}.[31,32] Fig. 2a shows a strong

absorption band of Zn_1-HDA at 299 cm^{-1}, which could be attributed to the Zn-N stretching mode. Additionally, the presence of a broad peak at ca. 342 cm^{-1} (Fig. 2a) is consistent with the emergence of a Co-N bond.[33] The energies of vibration modes within the solid, which are affected by the atomic arrangements, determine the FTIR peak positions.[34] The vibration peak shift is associated with the order of metal-ligand coordinate bond strength (i.e., Co-N > Zn-N).[35] In the infrared spectrum (Fig. 2a) of the bimetallic HDA with R = 0.33 [$Zn_{0.41}Co_{0.59}(C_3H_3N_2)_2$], the broadening of the peak could be linked to the increased presence and enhanced strength of Co-N bonds within the HDA structure. Moreover, the co-existence of the Zn-N and Co-N stretch confirms the chemical coordination between imidazole and metal ions in the structures of the HDAs. Furthermore, the higher bonding strength of bimetallic HDAs and Co_1-HDA compared to the Zn_1-HDA was verified by the N 1s high-resolution XPS spectra. As shown in Fig. 2b, the N atoms in the HDAs consist of pyrrolic N and pyridinic N at the binding energy of 399.9 eV and 399.0 eV, respectively.[36] After Co is incorporated into the Zn_1-HDA framework, the pyridinic N peak shifts to higher binding energy, indicating the stronger bond strength of the HDA structure. Hence, the total bond strength in the Zn-ZIF-4 HDA increases upon the substitution of Co for Zn.

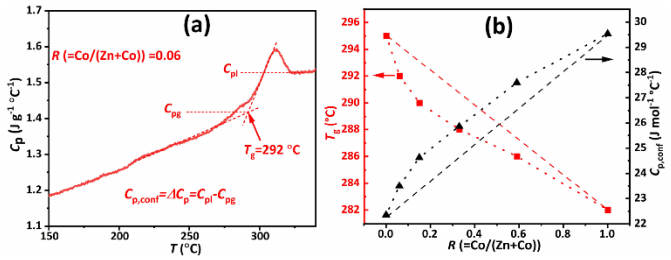

Fig. 3. (a) C_p curve for $Zn_{0.94}Co_{0.06}$-HDA at a heating rate of 10 °C min^{-1}. (b) The molar ratio R dependence of T_g and $C_{p,conf}$. Dotted lines: guides for the eyes. Dashed lines: Liner line connecting the two end-member compositions. The uncertainty of this method is around ±0.5 °C for T_g and ±0.5 J mol^{-1} $°C^{-1}$ for $C_{p,conf}$. Note that the error in T_g determination is relatively high, e.g., it accounts for about 25% of the T_g difference between the two samples with R = 0.00 and 0.15.

Glass transition occurs around the temperature at which the viscosity of the supercooled liquid is equal to 10^{12} Pa·s.[37-39] The onset of the glass transition during DSC measurement is termed the standard T_g.[37,39] To compare T_g, the HDAs are reheated to 340 °C at 10 °C min^{-1} to obtain the isobaric heat capacity (C_p) curves. As shown in Fig. 3a and Fig. S20, an endothermic peak belonging to the glass transition appears in all of the HDAs. In Fig. 3b and Table S2, it is seen that the T_g (282 °C) of Co_1-HDA is lower than that of Zn_1-HDA (295 °C). The molar ratio R dependence of the T_g for HDA shows a slightly negative deviation from a linear interpolation of the T_g values of the binary end-member phases (Zn_1-HDA and Co_1-HDA), known as the mixed-metal node effect.[14] Moreover, Fig. 3a illustrates the procedure used to determine $\Delta C_p = C_{pl}$ (the liquid heat capacity) − C_{pg} (the glass heat capacity).[18,38] ΔC_p is approximately equivalent to the configurational heat capacity ($C_{p,conf}$), regarded as a measure of the configurational degrees of freedom.[38] A positive deviation of $C_{p,conf}$–R relationship has been observed (Fig. 3b). The difference in $C_{p,conf}$ between the HDAs with R = 0.00 and 1.00 is approximately 7 J mol^{-1} $°C^{-1}$ (see the comparison in Table S2).

According to the topological model incorporating temperature dependent-constraints, T_g should be mainly determined by the interconnected structural units and the relative strengths of the different constraints.[40] In the ZIF-4 framework, the M node and the organic imidazole ring link together to form the MN_4 tetrahedron, which is the basic unit constituting the short-range structure.[10] Since both M-ZIF-4 (M = Zn or Co) materials are isostructural, the difference in the bond strength should account for their different T_g values. Through density functional theory calculations, the Zn-N bond energy of 2.075 eV is reported to be much lower than the Co-N bond energy of 2.834 eV.[34] This could be ascribed to the lower electronegativity of Zn (1.65) compared with that of Co (1.88).[24] Furthermore, the bonding of the linkers (i.e., Im) to the Zn^{2+} centers of Zn-ZIF-4 can be described by σ-bonding due to the specific $3d^{10}$ electron configuration. Additionally, the $3d^7$ electron configuration of Co^{2+} is responsible for the presence of additional ligand-to-metal π-bonding for Co-ZIF-4. The π-bonding could result qualitatively in stronger imidazolate-metal bonds.[41] Overall, the electronegativity and electronic structure of the metal ions could contribute to the disparity in the bond strength between Co-N and Zn-N.[14,42]

Based on topological constraint theory, the stronger bonds in the structure usually cause the higher T_g of materials.[43] However, the T_g of Zn_1-HDA with lower metal-bond strength is higher than that of Co_1-HDA. Therefore, the direct correlation between the bond strength in the HDAs and the observed variation in T_g is inconclusive. The T_g of the HDA system exhibits a negative trend as the R increases (see Fig. 3b). While the glass transition is primarily a dynamic phenomenon, its thermodynamic consequence is the freezing event of the configurational degree of freedom within the glass.[11] The reduction in polyhedral symmetry could result in a decrease in network connectivity[44], which is inversely correlated with the configurational degrees of freedom[18,34]. The anisotropic nature of the π-bonding in the Co electronic structure is expected to lower the symmetry of the CoN_4 tetrahedra.[45] In general, the stronger bond strength corresponds to a lower degree of symmetry[46]. Additionally, it has been found that the Zn-N bond is more ionic than the Co-N bond with a covalent character.[47] The stronger covalency in the Co-N bond reduces the CoN_4 tetrahedral symmetry.[48,49] Therefore, the presence of the Co-N bonds in the HDA framework lowers the tetrahedral symmetry of the HDA structure. The lower the tetrahedral symmetry is, the more the network is depolymerized, and hence, the higher the degree of the configurational freedom in the Zn,Co-HDAs is. This is confirmed by the dependence of $C_{p,conf}$ on the measured molar ratio R, which deviates positively from linearity (Fig. 3b), thereby leading to a nonlinear decrease of T_g with increasing R.

In this study, we discovered that introducing cobalt (Co) into the topological frameworks of the Zn-ZIF-4 HDA lowers its T_g value. The decreasing trend of T_g with substituting Co for Zn featured a negative deviation from linearity, i.e., the mixed-metal node effect occurs in the HDA. The FTIR, XPS and DSC results confirmed the connection between the T_g values and the

bonding nature between metal and nitrogen. The mixed-metal node effect on T_g could arise from the difference in the degree of configurational freedom due to the difference in tetrahedral symmetry, which is influenced by the electronic structure and M-nitrogen bonding nature. Our study provides insight into the mixed-metal node effect on the glass transition in the high-density amorphous phase of ZIFs. The insight helps us to develop meltable ZIF materials and to enhance their applications.

We thank the National Natural Science Foundation of China (No. 22175135). And ZD acknowledges the China Scholarship Council for support.

Conflicts of interest

There are no conflicts to declare.

Notes and references

1 R. Lin, M. Chai, Y. Zhou, V. Chen, T. D. Bennett and J. Hou, *Chem. Soc. Rev.*, 2023, **52**, 4149-4172.
2 M.-Z. Chen, J. Li, S. Liao, Y.-H. Guo, T. Liu, R.-F. Ma, T.-Y. Xie, W.-D. Liu, S.-X. Peng, X. Kuang, Z. Yin, Y. Zhao and M.-H. Zeng, *Angew. Chem. Int. Ed.*, 2023, e202305942.
3 Z. Yin, Y. Zhao, S. Wan, J. Yang, Z. Shi, S.-X. Peng, M.-Z. Chen, T.-Y. Xie, T.-W. Zeng, O. Yamamuro, M. Nirei, H. Akiba, Y.-B. Zhang, H.-B. Yu and M.-H. Zeng, *J. Am. Chem. Soc.*, 2022, **144**, 13021.
4 H. Tao, T. D. Bennett and Y. Z. Yue, *Adv. Mater.*, 2017, **29**, 1601705.
5 T. D. Bennett and S. Horike, *Nat. Rev. Mater.*, 2018, **3**, 431-440.
6 A. Qiao, T. D. Bennett, H. Z.Tao, A. Krajnc, G. Mali, C. M. Doherty, A. W. Thornton, J. C. Mauro, G. N. Greaves and Y. Z. Yue, *Sci. Adv.*, 2018, **4**, eaao6827.
7 J. Zhang, L. Longley, H. Liu, C. W. Ashling, P. A. Chater, K. A. Beyer, K. W. Chapman, H. Tao, D. A. Keen, T. D. Bennett and Y. Z. Yue, *Chem. Commun.*, 2019, **55**, 2521-2524.
8 L. León-Alcaide, R. S. Christensen, D. A. Keen, J. L. Jordá, I. Brotons-Alcázar, A. Forment-Aliaga and G. Mínguez Espallargas, *J. Am. Chem. Soc.*, 2023, **145**, 11258-11264.
9 A. Qiao, T. D. Bennett, H. Z.Tao, A. Krajnc, G. Mali, C. M. Doherty, A. W. Thornton, J. C. Mauro, G. N. Greaves and Y. Z. Yue, *Sci. Adv.*, 2018, **4**, eaao6827.
10 R. S. K. Madsen, A. Qiao, J. S. Sen, I. Hung, K. Z. Chen, Z. H. Gan, S. Sen and Y. Z. Yue, *Science*, 2020, **6485**, 1473-1476.
11 Q. Zheng, Y. Zhang, M. Montazerian, O. Gulbiten, J. C. Mauro, E. D. Zanotto and Y. Z. Yue, *Chem. Rev.*, 2019, **119**, 7848-7939.
12 T. D. Bennett, J. C. Tan, Y. Z. Yue, E. Baxter, C. Ducati, N. J. Terrill, H. H. Yeung, Z. Zhou, W. Chen, S. Henke, A. K. Cheetham and G. N. Greaves, *Nat. Commun.*, 2015, **6**, 8079.
13 J. Song, L. Frentzel-Beyme, R. Pallach, P. Kolodzeiski, A. Koutsianos, W. L. Xue, R. Schmid and S. Henke, *J. Am. Chem. Soc.,* 2023, **145**, **16**, 9273-9284.
14 R. S. K. Madsen, M. Stepniewska, Y. Yang, A. Qiao, W. M. W. Winters, C. Zhou, J. Konig, J. C. Mauro and Y. Z. Yue, *RSC Adv.*, 2022, **12**, 10815-10824.
15 R. Lin, X. Li, A. Krajnc, Z. Li, M. Li, W. Wang, L. Zhuang, S. Smart, Z. Zhu, D. Appadoo, J. R. Harmer, Z. Wang, A. G. Buzanich, S. Beyer, L. Wang, G. Mali, T. D. Bennett, V. Chen and J. Hou, *Angew. Chem., Int. Ed.*, 2022, **61**, e202112880.
16 C. Gao, Z. Jiang, S. Qi, P. Wang, L. R. Jensen, M. Johansen, C. K. Christensen, Y. Zhang, D. B. Ravnsbaek and Y. Z. Yue, *Adv. Mater.*, 2022, **34**, 2110048.
17 J. Yan, C. Gao, S. Qi, Z. Jiang, L. R. Jensen, H. Zhan, Y. Zhang and Y. Z. Yue, *Nano Energy*, 2022, **103**, 107779.
18 M. A. Ali, W. M. W. Winters, M. A. Mohamed, D. Tan, G. Zheng, R. S. K. Madsen, O. V. Magdysyuk, M. Diaz-Lopez, B. Cai, N. Gong, Y. Xu, I. Hung, Z. Gan, S. Sen, H. T. Sun, T. D. Bennett, X. Liu, Y. Z. Yue and J. Qiu, *Angew. Chem. Int. Ed.*, 2023, **135**, e202218094.
19 L. F. Beyme, P. Kolodzeiski, J.-B. Weiß, A. Schneemann and S. Henke, *Nat. Commun.*, 2022, **13**, 7750.
20 D. Saliba, M. Ammar, M. Rammal, M. Al-Ghoul and M. Hmadeh, *J. Am. Chem. Soc.*, 2018, **140**, 1812-1823.
21 M. A. Ali, J. Ren, T. Zhao, X. Liu, Y. Hua, Y. Z. Yue and J. Qiu, *ACS Omega*, 2019, **4**, 12081-12087.
22 W. Hume-Rothery, R. E. Smallman and C. W. Hayworth, The Structure of Metal and Alloys, Institute of Metals and the Institution of Metallurgists, London, 1969.
23 R. D. Shannon, *Acta Crystallogr., Sect. A: Cryst. Phys., Diffr., Theor. Gen. Crystallogr.*, 1976, **32**, 751-767.
24 A. L. Allred, *J. Inorg. Nucl. Chem.*, 1961, **17**, 215-221.
25 T. Panda, S. Horike, K. Hagi, N. Ogiwara, K. Kadota, T. Itakura, M. Tsujimoto and S. Kitagawa, *Angew. Chem. Int. Ed.*, 2017, **129**, 2453-2457.
26 J. Zhang, A. Qiao, H. Tao and Y. Z. Yue, *J. Non-Cryst. Solids*, 2019, **525**, 119665.
27 M. R. Ryder, T. D. Bennett, C. S. Kelley, M. D. Frogley, G. Cinque and J. C. Tan, *Chem. Commun.*, 2017, **53**, 7041-7044.
28 G. Jiang, C. Qu, F. Xu, E. Zhang, Q. Lu, X. Cai, S. Hausdorf, H. Wang and S. Kaskel, *Adv. Funct. Mater.*, 2021, **31**, 2104300.
29 K. Zou, P. Cai, X. Deng, B. Wang, C. Liu, Z. Luo, X. Lou, H. Hou, G. Zou and X. Ji, *Chem. Commun.*, 2021, **57**, 528-531.
30 Z. Du, D. Xiong, J. Qian, T. Zhang, J. Bai, Fang and H. Li, *Dalton Trans.*, 2019, **48**, 13753-13759.
31 M. R. Ryder, T. D. Bennett, C. S. Kelley, M. D. Frogley, G. Cinque and J. C. Tan, *Chem. Commun.*, 2017, **53**, 7041-7044.
32 M. R. Ryder, B. Civalleri, T. D. Bennett, S. Henke, S. Rudic, G. Cinque, F. Fernandez-Alonso and J. C. Tan, *Phys. Rev. Lett.*, 2014, **113**, 215502.
33 I. Nakagawa, T. Shimanouchi and K. Yamasaki, *Inorg. Chem.*, 1964, **3**, 772-773.
34 C. Wu, D. Xie, Y. Mei, Z. Xiu, K. M. Poduska, D. Li, B. Xu and D. Sun, *Phys. Chem. Chem. Phys.*, 2019, **21**, 17571-17577.
35 L. J. Boucher and J. J. Katz, *J. Am. Chem. Soc.*, 1967, **89**, 1340-1345.
36 L. Ge, Y. Yang, L. Wang, W. Zhou, R. De Marco, Z. Chen, J. Zou and Z. Zhu, *Carbon*, 2015, **82**, 417-424.
37 Y. Z. Yue, *J. Non-Cryst. Solids*, 2008, **354**, 1112-1118.
38 H. Liu, M. M. Smedskjaer, H. Tao, L. R. Jensen, X. Zhao and Y. Z. Yue, *Phys. Chem. Chem. Phys.*, 2016, **18**, 10887-10895
39 Y. Z. Yue, *J. Non-Cryst. Solids*, 2009, **355**, 737-744.
40 M. M. Smedskjaer, J. C. Mauro, R. E. Youngman, C. L. Hogue, M. Potuzak and Y. Z. Yue, *J. Phys. Chem. B*, 2011, **115**, 12930-12946.
41 S. Henke, M. T. Wharmby, G. Kieslich, I. Hante, A. Schneemann, Y. Wu, D. Daisenberger and A. K. Cheetham, *Chem. Sci.*, 2018, **9**, 1654-1660.
42 L. Frentzel-Beyme, M. Kloß, R. Pallach, S. Salamon, H. Moldenhauer, J. Landers, H. Wende, J. Debus and S. Henke, *J. Mater. Chem. A*, 2019, **7**, 985-990.
43 J. Kjeldsen, M. M. Smedskjaer, J. C. Mauro, R. E. Youngman, L. Huang and Y. Z. Yue, *J. Non-Cryst. Solids*, 2013, **369**, 61-68.
44 L. Meng, Q. Cheng, C. Kim, W.-Y. Gao, L. Wojtas, Y.-S. Chen, M. J. Zaworotko, X. P. Zhang and S. Ma, *Angew. Chem. Int. Ed.*, 2012, **51**, 10082-10085.
45 H. Thauern and R. Glaum, *Inorg. Chem.*, 2007, **46**, 2057-2066.
46 K. T. Moore, P. Söderlind, A. J. Schwartzand D. E. Laughlin, *Phys. Rev. Lett.*, 2006, **96**, 206402.
47 S. Sarkar, T. B. E. Gronbech, A. Mamakhel, M. Bondesgaard, K. Sugimoto, E. Nishibori and B. B. Iversen, *Angew. Chem. Int. Ed.*, 2022, **61**, e202202742.
48 P. C. Müller, C. Ertural, J. Hempelmann and R. Dronskowski, *J. Phys. Chem. C*, 2021, **125**, 7959-7970.
49 S. Mellaerts, J. W. Seo, V. Afanas'ev, M. Houssa and J.-P. Locquet, *Phys. Rev. Mater.*, 2022, **6**, 064410.

